

Imaging and Nulling with the Space Interferometer Mission

Torsten Böker¹ & Ronald J. Allen

Space Telescope Science Institute, 3700 San Martin Drive, Baltimore, MD 21218, U.S.A.

ABSTRACT

We present numerical simulations for a possible synthesis imaging mode of the Space Interferometer Mission (SIM). We summarize the general techniques that SIM offers to perform imaging of high surface brightness sources, and discuss their strengths and weaknesses. We describe an interactive software package that is used to provide realistic, photometrically correct estimates of SIM performance for various classes of astronomical objects. In particular, we simulate the cases of gaseous disks around black holes in the nuclei of galaxies, and zodiacal dust disks around young stellar objects. Regarding the first, we show that a Keplerian velocity gradient of the line-emitting gaseous disk — and thus the mass of the putative black hole — can be determined with SIM to unprecedented accuracy in about 5 hours of integration time for objects with H α surface brightness comparable to the prototype M 87. Detections and observations of exo-zodiacal dust disks depend critically on the disk properties and the nulling capabilities of SIM. Systems with similar disk size and at least one tenth of the dust content of β Pic can be detected by SIM at distances between 100 pc and a few kpc, if a nulling efficiency of 10^{-4} is achieved. Possible inner clear regions indicative of the presence of massive planets can also be detected and imaged. On the other hand, exo-zodiacal disks with properties more similar to the solar system will not be found in reasonable integration times with SIM.

Subject headings: space vehicles — techniques:interferometric — methods:numerical — circumstellar matter — galaxies:active

1. Introduction

For certain areas of current astronomical research, such as the detection and mass determination of black holes in galactic nuclei, spatial resolution is the main limitation. For others, e.g. the case of extrasolar planets, the challenge is to detect very faint signals in the presence of an overwhelmingly bright star. Interferometry from space has the potential to overcome both of these obstacles: it has no fundamental limit to spatial resolution, and interferometric nulling is by far the most powerful method to suppress unwanted light from a bright point source.

The Space Interferometer Mission (SIM) will be the first mission to demonstrate the feasibility of this new and exciting technology. Scheduled for launch in 2005, SIM is the first new mission of NASA's ORIGINS program after SIRTF. It is designed primarily for astrometry at the μ arcsec-level. However, SIM may also have significant capabilities for synthesis imaging. In terms of spatial resolution, SIM with a maximum baseline of 12 m promises at least a factor of six improvement over the Hubble Space Telescope (HST).

¹Affiliated with the Astrophysics Division, Space Science Department, European Space Agency

In this paper, we discuss the potential of SIM to significantly improve upon current observational limits in two specific astronomical cases, namely line-emitting gas disks rotating around black holes in galactic nuclei, and continuum zodiacal dust disks around nearby stars. In the next section, we will describe how SIM performs synthesis imaging, and discuss some aspects and limitations that will affect the observations. Section 3 gives an overview of the capabilities of the code which we use to simulate various classes of model sources. Input models and first results of simulations for the two examples mentioned above are described in Sections 4 and 5. We discuss and summarize our findings in Section 6. Appendices describe the basics of interferometric imaging, and the simulation of measurement errors in our models, respectively.

2. Synthesis imaging with SIM

As of November 1998, certain aspects of SIM design which are important for synthesis imaging have not yet been finalized. The most important of these is to have a sufficiently complete range of baseline spacings available. For the purpose of this paper, we assume that SIM will have baselines between 0.5 and 12 m in increments of 0.5 m, similar to the original design (see Allen *et al.* 1997 for an overview). With these capabilities, SIM will be well suited to perform reliable synthesis imaging for a wide range of complicated sources.

The basic “measurement” for synthesis imaging consists of determining the amplitude and phase of the interference fringes for a given baseline and spacecraft orientation. These two quantities together form the “complex visibility”. In short, the signal of the two interfering beams on the detector depends on the path difference or “delay” between them. The interference pattern is a cosine wave whose amplitude and phase are the desired observables. If the path delay is accurately known and controllable, the complex visibility can be determined by “scanning” the delay. Repeating this measurement for a large number of baselines then allows a more or less complete reconstruction of the sky brightness distribution, depending on its complexity. In Appendix A we describe in more detail the operation of the interferometer in terms of Fourier optics. Here, we concentrate on the performance of SIM for astronomical targets.

2.1. Observing procedure

1. The relative length of the baseline vector is monitored and controlled with an internal laser metrology system, while its exact length and orientation are determined by observing nearby bright stars. Pointing stability is achieved with two additional guide interferometers.
2. The science interferometer is aligned such that the phase center (zero delay, or white light fringe) coincides with the position of a reference star.
3. The delay lines are adjusted such that the phase center moves to the science target which has to lie in the 15° field of regard of SIM. In the case of astrometric measurements of a point source *position*, the only interesting observable is the delay needed to maximize the white light fringe. This determines the position of the source with respect to the reference star. Identification of the white light fringe is unambiguous since the light is spectrally dispersed: only the central fringe will show no phase shift for all spectral channels.
4. In the case of an extended source that is to be imaged, the complex visibility is measured with the delay modulation method (Shao & Staelin (1977)) or some variation thereof, which we describe

in Appendix B. Since the signal is spectrally dispersed, the complex visibilities are measured simultaneously for all spectral channels. This is the basis for the spectral synthesis technique that we describe in Section 2.4.

5. Baseline length, orientation, and wavelength determine the (u,v) -coordinate to which the complex visibility is assigned. The wavenumbers u and v are defined as $u \equiv B_x/\lambda$ and $v \equiv B_y/\lambda$, where B_x and B_y are the baseline projections onto the x and y axes of the reference frame. The measurement is repeated for as many baselines as necessary to sufficiently fill the (u,v) -plane.² The image can then be recovered from the (u,v) -data by Fourier-inversion, and spurious responses removed by computer restoration.

2.2. Instrumental Parameters

2.2.1. Spatial resolution

The spatial resolution of a synthesis imaging observation is not a priori defined. A diffraction-limited filled aperture with a diameter of $D = 12\text{ m}$ operating at a wavelength of $\lambda = 500\text{ nm}$ has a central response FWHM of $1.22\lambda/D = 0.01''$. In contrast, the final resolution of an image reconstructed from a set of interferometer measurements is not uniquely defined. By varying the weighting of the individual (u,v) -coordinates, or even removing some baselines completely, one can put more or less emphasis on certain spatial frequencies in the reconstruction, and thus change the effective resolution, even *after* the data are taken.

For example, using a Gaussian weighting which falls to 0.25 at the longest (12 m) baseline results in a FWHM of 7 mas with very low sidelobes. Another option is to use only a narrow ring of long baselines which yields a resolution almost twice as high as that of the full telescope. This fact is regularly exploited in “aperture masking” observations of bright double stars where collecting area is not an issue, but the highest possible resolution is required. Therefore, SIM will yield a resolution for synthesis imaging anywhere between 5 and 10 mas, depending on the actual distribution of measurements in the (u,v) -plane, and the weighting algorithm used.

2.2.2. Field of View

The field of view (FOV) is limited by the coherence length of the light, $l = c\tau = c/\Delta\nu = \lambda^2/\Delta\lambda$, where τ is the coherence time of the light, c is the speed of light, and $\Delta\nu$ is the bandwidth of the filter used for the observations. It can be easily calculated as the product of the spectral and spatial resolutions, which can be seen as follows: while the path lengths from the two interferometer elements are assumed to be equal in the center of the field, an angular separation Θ from the center along the baseline vector \vec{D} results in a path difference $\Theta \cdot D$. As long as this difference is small compared to $l = \lambda^2/\Delta\lambda$, the fringe contrast will not be affected. Thus, $\Theta < \frac{\lambda}{D} \cdot \frac{\lambda}{\Delta\lambda}$, or $\Theta < R_{\text{spatial}} \cdot R_{\text{spectral}}$. For example, a 10 nm wide channel at $\lambda = 600\text{ nm}$ would result in a FOV of $0.6''$. Any single baseline has a FOV that forms a $0.6''$ wide, long strip on the sky that is positioned perpendicular to the baseline. However, as the baseline rotates, sources along

² The exact meaning of “sufficiently” is a non-trivial problem and depends critically on the (unknown) source structure. This is the reason why detailed source modeling is needed to predict the imaging performance of any interferometer.

the strip more than $0.6''$ away from the center will appear and disappear in the FOV, thus affecting the measurements in an unpredictable way. In order to avoid this confusion, SIM will have a circular aperture stop in its optical path.

There is yet another constraint that sets even tighter limits on the FOV, namely, the need to avoid aliasing. Especially for a complicated source structure or crowded field this can be a major limitation on any deconvolution algorithm, since the sum of the grating rings of all the sources in the field can — and will — mimic fake sources, as will be demonstrated in Section 5.4. Unless a priori knowledge about the source structure exists, aliasing must be avoided for reliable source reconstruction. This means that in practice the SIM FOV is limited to a circle with a diameter of $0.2''$, which can be seen as follows. The position of the first grating ring of a point source in the field is determined by the spacing of the baselines. In the case of 0.5 m increments, the grating ring has a *radius* of $10/0.5=20$ times λ/D or $0.2''$. To make sure that no aliasing occurs from any source inside the FOV, it has to be limited to a *diameter* of $0.2''$. All of our simulations in this paper, however, have been carried out with a FOV of $0.3''$ in order to demonstrate the above effects.

Figure 1 shows a possible (u,v) -coverage obtained with 170 measurements and the resulting point spread function (PSF) or “dirty beam”. Here, and in all the simulations that are described in this paper, we have set the longest baseline to 10 m, which corresponds to the requirement of the original SIM design. The current design offers a maximum baseline of 12 m. The grating rings in the PSF described above are clearly visible. The number of samples in the (u,v) -plane in Fig. 1 is twice the number of measurements made. This is because any astronomical object has a purely real brightness distribution, so the mutual coherence function of the incoming wavefront is hermitian. Therefore, once the complex visibility of point (u,v) has been measured, its conjugate can be entered at point $(-u,-v)$. In addition, different from the case of radio interferometry, the total flux of the source is determined during every visibility measurement. This gives the value at the origin of the (u,v) -plane (the “zero spacing”) to high accuracy.

The “noisy” residuals around the central peak of the PSF are due to the incomplete (u,v) -coverage. Since, however, the (u,v) -coordinates of the SIM measurements are defined with extremely high precision, the shape of the PSF can be *calculated* very accurately and without the uncertainties and noise of an actual measurement. It is this precise knowledge of the PSF that makes SIM such a powerful imager, since the success of deconvolution algorithms like CLEAN or the Maximum Entropy Method (MEM) is limited by the knowledge of the PSF.

The accuracy of the “raw” synthesized image before deconvolution depends in a complicated way on several parameters, including the noise properties and flux distribution of the source, the stability of the phase measurements, and the actual (u,v) -coverage. In order to investigate these issues in detail, we have developed a software toolkit which we will describe in Section 3.

2.2.3. *Sensitivity*

Jumping ahead, we list here the results of the simulations described in sections 4 and 5 in order to provide an estimate of typical integration times needed to perform synthesis imaging of extended astronomical objects.

The surface brightness threshold for making scientifically useful images with SIM in the continuum band from 500-800 nm is $SB_c \approx 0.3$ mJy/ \square'' which corresponds to $m_V = 17.7/\square''$. Under the same

conditions an emission line such as H α can be imaged in a narrow (4 nm was assumed in the simulations) band with a threshold surface brightness of $SB_l \approx 2.5 \times 10^{-14}$ ergs/cm 2 /sec/ \square'' . A full synthesis with SIM will take typically 4 – 6 hours of on-target integration time for sources at these brightness levels. During this time, 150 – 200 different baselines and baseline orientations will be observed. Observations can of course be repeated to increase the sensitivity.

These sensitivities can be achieved even in the presence of point sources up to V=12 in the field of view using the nulling imaging mode discussed in the next section.

2.3. Imaging in nulling mode

Because of its unprecedeted baseline stability, SIM has great potential for interferometric nulling of point sources. One of the SIM beam combiners will introduce an achromatic 180° phase shift in one of the inteferometer arms by polarization inversion, thus eliminating the light from a point source that is located at the phase center. This capability is a programmatic technology demonstration requirement. The experience gained is crucial for the design of future space missions that are aimed at the detection of extra-solar planets, like e.g. the Terrestrial Planet Finder (TPF). The requirement for SIM is to reach a nulling efficiency of 10^{-4} . Many interesting science programs intend to use this capability to determine the spatial extent of objects like stars or supernova shells by measuring the light leakage around the phase center.

In this paper, we will describe another mode of observation, namely synthesis imaging in nulling mode. In Section 5, we will discuss the specific features of this technique for the case of exo-zodiacal dust disks.

2.4. Spectral synthesis imaging

Since SIM is designed to perform astrometric measurements in a dispersed fringe mode, it has a built-in spectroscopic capability. That is to say, the amplitude and phase of an object's wavefront are monitored simultaneously at a number of different wavelengths. Since the same physical baseline translates into different (u,v) -coordinates at different wavelengths, this information can, in principle, be used to increase the (u,v) -coverage. This method is usually referred to as spectral synthesis imaging.

Spectral synthesis has one major caveat: the implicit assumption in the reconstruction of the source is that its *structure does not change with wavelength*. In the optical regime this assumption is far from safe. In fact, it is often plain wrong, especially when strong emission lines are present in the bandpass considered. That does not mean that one cannot use spectral synthesis with SIM at all. There are classes of objects for which the above assumption is acceptable. For example, in the case of zodiacal disks around solar-type stars, it may be reasonable to assume that the structure of the source does not vary strongly over the SIM passband, since it is observed only in reflected starlight. We will present the results of spectral synthesis simulations for exo-zodiacal disks in Section 5.

3. SIMSIM — a software toolkit

In order to simulate the imaging capabilities of SIM, we have developed SIMSIM, a software package written in the Interactive Data Language (IDL) environment. The motivation was to obtain realistic performance estimates for a variety of target sources, and to develop optimal observing strategies. The principal steps carried out during a simulation are illustrated in Fig. 2.

In brief, a model source distribution is put on a finely-sampled grid (typically 256×256 pixel). For simplicity, the field center is assumed to be the center of rotation of the spacecraft during the synthesis imaging, and no effort has been made so far to account for possible pointing instabilities. The mutual coherence function of the source wavefront is calculated via a Fast Fourier Transform (FFT), and sampled on the (u,v) -coordinates observed by SIM. Noise is added, and the actual phase and amplitude retrieval process is simulated. The details of this algorithm are described in Appendix B. So far, we have incorporated photon noise according to Poisson statistics, and random phase calibration errors with an amplitude of up to 0.5° . A final Fourier inversion of this sampled and corrupted data then gives the “dirty” image. The PSF is calculated by transforming a mutual coherence function of unit amplitude and zero phase at each (u,v) -sample point of the observation. Deconvolution algorithms like CLEAN or the Maximum Entropy Method (MEM) can then be applied to minimize the effects of the incomplete (u,v) -coverage.

The nulling capability of SIM is modeled as follows. Before the noise is added to the source wavefront, its amplitude A (at each (u,v) -coordinate) is reduced by most of the amplitude A_c of the source at the phase center $u = v = 0$:

$$A_{\text{nulled}} = A - A_c \cdot (1 - \epsilon) \quad (1)$$

where ϵ denotes the accuracy to which nulling can be achieved. For SIM, ϵ is expected to be around 10^{-4} . It is limited by stray light due to imperfections in the optical elements and by the stability of the pathlengths. The phase of the wavefront is set to zero, resulting in an intrinsically symmetric source reconstruction. The reason for the loss of phase information is that the delay cannot be modulated without losing the null: once the light is minimized, the delay lines have to be kept as stable as possible. The reduced amplitude of the signal results in lower photon counts on the detector which, in turn, reduces the poisson noise.

Equation 1 ensures that the total flux in the reconstructed image is equal to the flux in the whole field-of-view **except for the central pixel** which, in the simulations, contains the flux of the nulled star. This is, of course, known for the models. However, in a real observation, such *a priori* information on the exact value of A_c does not exist. It is only possible to measure the total flux – including the central source – by doing a standard observation in the direct beam combiner. An iterative approach will be necessary, which adds an appropriate **constant** to each amplitude measurement; this constant is an estimate of the total flux in the field, minus the flux from the central source. If this value is chosen correctly, the reconstructed image will be zero at the phase center.

Since the model sources are intrinsically constructed on a regular grid, as are the (u,v) -coordinates of the “measurements”, there is no need for gridding procedures in our code. However, real sources and real observations will not be so conveniently organized, so that in order to fully model the SIM observations, weighting and gridding algorithms will have to be implemented. This work is currently underway.

Figure 3 illustrates the Graphical User Interface (GUI) of SIMSIM. The top panel allows the user to select between a number of model sources and to choose various observational parameters of SIM such as (u,v) -coverage, spectral resolution, etc. The intermediate steps of the simulation are displayed in the four graphics windows. All results can be saved in postscript format for printing or in FITS format for further

work with IDL or any other data analysis environment. In the following sections we use SIMSIM to model the capabilities of SIM to image two interesting classes of astronomical objects.

4. Black holes in galactic nuclei

Black holes have been detected convincingly in at least a dozen galaxies, both active and quiescent. The techniques for such detections are multifold (see Kormendy & Richstone 1995 for a review), but have concentrated on the dynamics of the gas and stars in the neighborhood of the black hole.

Stellar kinematical studies are often hampered by uncertainties regarding the stellar velocity dispersion anisotropy, and the need for high spatial resolution in connection with intrinsically low surface brightness makes such measurements very challenging even with HST. However, some galaxies have circumnuclear disks of ionized gas which provide a more favorable tool for black hole detection. The emission lines from the ionized gas are bright and have large equivalent width, and the dynamical state of the gas is relatively simple; its rotation curve directly yields the black hole mass.

As a starting point for our discussion, we have chosen M 87 as the best known example for such a line-emitting gaseous disk. The next section briefly describes our input model for M 87.

4.1. An example: M 87

M 87, a dominant giant elliptical galaxy in the Virgo cluster, is the prototype for galaxies that harbour a central black hole, the presence of which is revealed by a line-emitting gaseous disk. The nucleus of M 87 has been imaged with HST in both continuum (Lauer *et al.* 1992) and line emission (Ford *et al.* 1994, and the ionized gas has been studied spectroscopically in great detail (Harms *et al.* 1994, Macchetto *et al.* 1997, Marconi *et al.* 1997) We thus have a fairly clear picture of the properties of the nuclear gas disk. Table 1 summarizes the parameters we used to construct a realistic model flux distribution for the gaseous disk around the central black hole in M 87. The H α surface brightness over the central 0.25" of our model is $1 \cdot 10^{-12}$ ergs/cm 2 /Å \square ", as derived from the observed [SII] flux (Harms *et al.* 1994) and an assumed line ratio of [SII]/(H α +[NII]) = 4. The gas is assumed to show Keplerian rotation according to

$$\left(\frac{v_c}{100 \text{ km/s}}\right)^2 = 0.08869 \cdot \frac{\text{Mpc}}{d} \cdot \frac{M_\bullet}{10^6 M_\odot} \cdot \frac{\text{arcsec}}{r} \quad (2)$$

where M_\bullet denotes the black hole mass, r the angular distance from the center, and d the distance to the galaxy. The numbers listed in Table 1 then result in the rotation curve shown in Fig. 4.

The H α emission from the rotating disk would appear in a range of spectral channels, according to the Doppler shift of the gas velocity projected along the line of sight. For the above parameters, a (hypothetical) diffraction-free 10m-telescope in space, equipped with an integral field spectrometer with 4 nm wide channels, would see the source as in Fig. 5. Here, we have convolved the “true” flux distribution of the M 87 model with the “clean beam”, a Gaussian fitted to the central part of the PSF. While the central, unresolved continuum source appears in all channels, the appearance of the H α emission depends on parameters like channel width, black hole mass, inclination of the disk, etc.

To demonstrate the power of our analysis tools, we present in the next section what can be expected from SIM observations of M 87 and similar sources.

4.2. Results of the SIMsimulations

In Fig. 6, we present a few examples of our simulations that are intended to give an impression of what imaging with SIM can do in this context.

The first row of the left panel again shows those channels of our M 87 model containing H α emission. The channels again are 4 nm wide and centered at 554, 558, and 662 nm, respectively³. The second row shows the result of the direct Fourier inversion of the complex visibilities measured by SIM. The (u,v) -coverage was the same as in Fig. 1, and the integration time was 100s per measurement, for a total on-source integration time of about 5 hours. The nominal SIM throughput of 0.3 was assumed. We added photon noise to the measurements according to Poisson statistics. The third row shows the results after 200 iterations with the MEM algorithm. The emission structure of the high velocity gas is well recovered. The same is true for the H α intensity profile, as shown in Fig. 7.

The spatial extent of the H α emission in each channel provides valuable information on the velocity gradient, and thus the black hole mass. This is demonstrated in Fig. 8, where we have run the same simulation as described above, but for various black hole masses M_\bullet . We show only the blueshifted wing of the H α emission for values of $M_\bullet = 2, 3$, and $4 \times 10^9 M_\odot$. The SIM observations are very sensitive to the value of M_\bullet , a direct consequence of the linear relationship between black hole mass and radial distance in a Keplerian rotation curve, cf. eq. 2. However, it should be stressed that in practice fitting procedures are required to solve for all the free model parameters including black hole mass, disc inclination, and the actual distribution of disk surface brightness.

We emphasize that no attempt has been made to optimize the deconvolution process. For example, the stability and convergence of MEM can be greatly improved by using “a priori” knowledge about the source structure. However, in order to better be able to compare the results for different source models, we have — for all the simulations in this paper — started the MEM deconvolution with an empty array, and stopped after 200 iterations. For the real SIM observations, one would make every effort to optimize the deconvolution strategy for each individual dataset. This is, in fact, another area where future simulation work with SIMsim will be useful. However, it is our experience that if no trace of the source structure is evident in the direct Fourier inversion, no improvement can be expected from deconvolution, regardless of the algorithm employed. Thus, the quality of the data can be most directly judged from the direct Fourier inversion itself, before any restaoration.

4.3. Is there more than M 87?

An important goal of SIMsim is to define requirements on various aspects of the SIM spacecraft. As an example, what is the minimum spectral resolution of the SIM beam combiner that allows observations such as the one discussed here? Certainly, the channel width must not be smaller than the wavelength shift of the emission line under observation at a distance of at least one resolution element from the center. This, of course, depends on the black hole mass and the distance to the host galaxy. In Fig. 9, we have plotted the limiting black hole mass (i.e. the minimum mass that causes a shift of the H α emission of at least one spectral resolution element at an angular separation of two spatial resolution elements (0.02'') from the

³We have masked the central continuum source in these plots for better display only; the observation was not simulated in nulling mode.

center) as a function of the distance to the host galaxy for a number of possible SIM spectral resolutions and disk inclinations. For example, with 1 nm wide spectral channels (dotted lines), SIM can potentially detect $10^8 M_\odot$ black holes up to a distance of ≈ 80 Mpc, if the disk has an inclination $i \leq 20^\circ$. Whether the H α -flux in cases different from M 87 is sufficient to acquire a high signal-to-noise ratio in a reasonable amount of time is more uncertain.

5. Exo-zodiacal disks

Circumstellar dust disks are commonly thought to provide the material for planet formation. The structure of such disks is therefore important for our understanding of the processes that lead to the formation of planetary systems. Many searches have been started for such disks, most of which are based on coronographic observations and concentrate on stars with a high IR-excess as measured by the IRAS satellite (e.g. Smith, Fountain, & Terrile 1992). Until most recently, however, only one unambiguous detection of a circumstellar dust disk outside the solar system had been reported, namely the β Pic system. From modeling the β Pic disk, Kalas & Jewitt (1996) found that it is the uncommonly large scattering cross-section of the dust particles that makes β Pic a special case. If there were other nearby systems like β Pic, they would have been detected regardless of the disk inclination. Kalas & Jewitt (1996) conclude that at least an order of magnitude improvement in the suppression of the stellar light is needed to detect more “normal” circumstellar disks, i.e. with scattering cross section less than a tenth of that in β Pic.

SIM, with its interferometric nulling capability, differs from groundbased coronagraphic observations in a number of ways:

1. The starlight suppression in SIM is not limited by atmospheric seeing or the efficiency of an adaptive optics system, but only by the quality of the optical elements and the pathlength stability.
2. The high spatial resolution of SIM allows the detection of disks much smaller than that in β Pic, and SIM can therefore image such systems to greater distances d . In fact, SIM’s ability to detect exozodiacal disks increases with d , as long as the disk fills the 0.2'' FOV of SIM. This somewhat surprising behavior is due to the fact that the surface brightness of the disk varies only slightly with d , so its total signal on the SIM detector will stay more or less constant. The signal from the star, on the other hand, decreases as $1/d^2$, so that the noise contribution from the nulling residuals of 10^{-4} become less important. In addition, the further away the star is, the more it resembles a true point source. This will reduce light leakage around the null, which is also a source of photon noise even for a perfect nulling beam combiner.
3. Since all phase information in the nulling process is lost, the source after reconstruction *always* appears symmetric. That means that eventual asymmetries in the disk can not be recovered.
4. Aliasing due to the incomplete sampling of the mutual coherence function can sometimes mimic companion stars or planets.

In what follows, we investigate the SIM potential for the detection of zodiacal disks and specifically address the points listed above.

5.1. The model

We use a simple model of a circumstellar dust disk, based on the zodiacal emission of the solar system (Reach *et al.* 1996, Traub 1998). The particle number density of the solar system zodiacal dust cloud can be well modeled by the expression

$$\rho = \rho_0 \cdot r^{-\alpha} \cdot e^{-\beta \cdot (z/r)^\gamma} \quad (3)$$

where r is the in-plane radial distance from the center, z is the modulus of the perpendicular-to-plane distance (in AU), $\alpha = 1.4$, $\beta = 3.26$, and $\gamma = 1.02$. We treat the scattering efficiency of the dust particles as a flux scaling parameter, and we assume isotropic scattering. In what follows, we investigate the two limiting cases of a face-on ($i=90^\circ$) and edge-on ($i=0^\circ$) orientation of the disk.

The radial surface brightness distribution of the face-on disk can be derived from integrating the volume density. For $\gamma = 1$ it is given by the expression

$$\sigma_{(i=90^\circ)} = C \cdot \sigma_1 \cdot r^{-\alpha+1}. \quad (4)$$

Here, C is a scaling factor that characterizes the scattering efficiency of the dust particles in an exo-solar system relative to the solar system. The normalization constant σ_1 is the surface brightness of the face-on disk, as seen from outside the solar system, at a distance of 1 AU from the sun. Assuming isotropic scattering, this number is (at $\lambda=550$ nm)

$$\sigma_1 = 0.13 \text{ MJy/sr}. \quad (5)$$

An approximate ratio of the surface densities of the edge-on and face-on directions at a given value for r can be obtained by ratioing the characteristic scale heights of the z -direction and along a tangent to r in the plane:

$$e/f = \beta^{1/\gamma} \cdot \sqrt{e^{2/\alpha} - 1} \approx 5. \quad (6)$$

An approximation to the edge-on surface brightness distribution is therefore

$$\sigma_{(i=0^\circ)} = C \cdot e/f \cdot \sigma_1 \cdot r^{-\alpha+1} \cdot e^{-\frac{\beta z}{r}}. \quad (7)$$

where $\gamma \approx 1$ is used. Figure 10 gives a visual impression of the model in both the face-on and edge-on case. The spectrum of the dust in the wavelength range discussed here (500 – 1000 nm) is assumed to be that of a black body with the temperature of the central star.

5.2. β Pic — the showcase

In this section, we investigate the question whether SIM is capable of finding other systems like β Pic, should they exist. In this context, we define “ β Pic-like” as having about 1000 times the dust content and surface brightness of the solar system, i.e. $C=1000$, without any detailed modeling of the specific properties of β Pic itself.

As mentioned above, the SIM performance in terms of imaging of circumstellar disks is very limited for nearby systems, but improves with increasing distance, as long as the disk fills the FOV. For example, the β Pic disk itself is impossible to image with SIM, because even with 10^4 nulling, the photon noise of the remaining light from β Pic would make the detection of the faint disk emission impossible. Figure 11 demonstrates the increasing sensitivity of SIM up to distances of 1 kpc.

Again, we note that no attempt has been made to optimize the restoration procedure in order to avoid additional degrees of freedom. As can be seen in Figure 11, SIM can easily detect β Pic-like systems up to a distance of about 1 kpc, beyond which our model disk no longer fills the SIM FOV and its total flux drops rapidly. This distance limit depends linearly on the extent of the disk, for which we have assumed a value of 100 AU. This is a somewhat arbitrary number, chosen such that the angular diameter at a distance of 1 kpc is $0.2''$, equal to the SIM FOV. The central star is assumed to be of solar type ($M_V=5$).

5.3. Can SIM find other solar systems?

The above results change dramatically if systems with lower dust contents than β Pic are considered. The dust content of our model disks is parametrized by the constant C in eq. 7. Figure 12 summarizes our results on studying various values for C . Disks with more than a tenth of the dust content of β Pic can be detected with SIM. However, it is evident that zodiacal disks similar to that of the solar system will not be found with SIM, regardless of their distance or inclination.

5.4. What are the clumps?

It is interesting that in all of our reconstructions, the disk structure after deconvolution appears much more clumpy than the smooth input model. In fact, when looking at the results, one might in many cases think to have found a number of planets. These “clumps” are artefacts of the restoration process on our incomplete (u,v) -data. While the sidelobe pattern itself is known to high accuracy, the poisson noise associated with the signal does not have the shape of the PSF. Spikes in the noise distribution create residuals that are mistaken as real source structure by any deconvolution algorithm. The fact that the clumps are indeed randomly distributed can be seen when comparing three independent simulations of the face-on zodiacal disk of a β Pic-like system at 1 kpc and a nulling efficiency of $\epsilon = 10^{-4}$ in Figures 11, 12, and 13, which only differ in their random photon noise. A repetition of the observation would allow identification of such spurious objects.

5.5. How critical is the Nulling?

In order to investigate the effects of a degradation of the SIM nulling capability, we have run a series of simulations with different values for ϵ , the nulling efficiency in eq. 1. Figure 13 demonstrates that for a β Pic-like system at 1 kpc, the most favorable case in all of the simulations we have run so far, SIM could detect the disk even if it had only $\epsilon = 10^{-3}$. However, anything worse than that would not suppress the starlight sufficiently even at such high distances. We conclude that in order to be a powerful search engine for exo-zodiacal disks, SIM needs to achieve at least $\epsilon = 10^{-4}$, and anything better would improve the performance considerably.

5.6. Planetary Gaps

A massive planet — if present — is believed to sweep up any inward-spiraling debris and thus cause a dust-free region in the circumstellar disk inward of the planet’s orbit. Such an “inner gap” is believed

to exist in the β Pic-system, as inferred from its spectral energy distribution (Lagage & Pantin 1994), but the gap has never been directly imaged owing to the large radius which is masked out by coronographic instruments.

With its high spatial resolution and sensitive nulling, SIM is able to directly image possible inner clear regions in exo-zodiacal systems. This is demonstrated in Fig.14 where we have investigated the case of a β Pic-like disk at a distance of 500 pc with and without a 20 AU inner clear region. Clearly, the signature of the disk depends on its size and the distance to the system, but a 20 AU radius gap would be detectable in systems as distant as 1 kpc. Here, we just want to illustrate the intriguing prospect of directly imaging such gaps (and later, possibly the planets that cause them).

6. Summary

We have built an interactive software package that enables us to perform numerical simulations of imaging observations with SIM. The results obtained so far can be summarized as follows:

1. SIM, with a spectral resolution of 1 nm, can resolve the velocity structure of line-emitting gaseous disks around black holes in the centers of nearby galaxies down to black hole masses of $10^8 M_\odot$ at distances up to 100 Mpc. With this resolution, SIM is in principle capable of determining the mass of the black hole to 10% accuracy. The necessary integration time depends on the H α -flux from the disk; for cases like M 87, about 5 hours is sufficient. A coarser spectral resolution of SIM would constrain the accessible parameter space for quantities such as distance, black hole mass, or disk inclination.
2. Given a nulling efficiency of 10^{-4} , SIM can image zodiacal disks with dust contents similar to that of the β Pic-system with high signal-to-noise ratio in about 5 hours of integration time. The limiting distance depends only on the angular size of the disk, which should be no smaller than 0.1''.
3. Inner clear regions in the disk can be directly detected and imaged with SIM for systems at a distance of up to 1 kpc provided that the dust-free region has a radius of at least 20 AU.

We are grateful to R. van der Marel for his advice on the black hole simulations, and to W. Traub for his expertise on the zodiacal disk model. We also would like to thank S. Unwin, M. Colavita and M. Shao for their interest in and continued support of this project. The work described in this paper is carried out at STScI with financial support from the SIM project at the Jet Propulsion Laboratory (JPL).

A. The Fourier optics of SIM

The idea that an interferometer could be constructed to measure the angular diameters of stars is usually credited to Fizeau (1868), although no details were provided in that particular reference. Twenty years later, Michelson (1890) took it up and, another 30 years later with Pease, constructed the now-famous stellar interferometer on the 100-inch telescope (Michelson & Pease 1921). Figure 15 shows a sketch of the original drawing from that paper, to which we have added symbols indicating the spacing L of the outrigger mirrors and the spacing D of the mirrors at the telescope aperture which direct the light to the primary mirror. Variations of this sketch appear in many introductory textbooks on physics and astronomy.

The image of a star in the focal plane of the stellar interferometer is crossed by interference fringes, as shown in cross section in Fig.16, where some additional parameters are defined: the *fringe amplitude* A , the *fringe period* $\Delta\theta$ and the *fringe phase* ϕ . In this picture the average signal from the star has been normalized to 1. The overall size of the Airy pattern is set by the aperture formed by the cascade of small reflecting mirrors which direct the light to the telescope primary mirror.

As is well known from the general theory of wave diffraction, this Fraunhofer diffraction pattern in the focal plane of the telescope is the square modulus of the Fourier Transform of the distribution of illumination (in amplitude and in relative phase) over the aperture. The expression for the stellar interferometer can be derived in a straightforward way, at least in one dimension, by starting from the result for the single-slit diffraction problem. We then use standard theorems from the theory of Fourier Transforms, in particular the shift theorem and the convolution theorem, and apply them to a plane wavefront over the entrance aperture (pupil). In this way it is straightforward to show that the final Fraunhofer pattern for an unresolved star is the square modulus of

$$\begin{aligned} M(u) &= F(u - u_0) \times G(u - u_1) \\ &= 2 \operatorname{sinc}(\pi a(u - u_0)) \cos(\pi(Du - Lu_0)) \end{aligned} \quad (\text{A1})$$

with $\operatorname{sinc}(x) \equiv \sin(x)/x$, and $u \equiv \sin\phi$, ϕ being an angle as defined in Fig.16. This is the product of the pattern $F(u) = \operatorname{sinc}(\pi a(u - u_0))$ for a single slit of width a offset to $u_0 = \sin\phi_0/\lambda$, and the pattern $G(u) = 2 \cos(\pi D(u - Lu_0/D))$ for a very thin double slit offset to $u_1 = Lu_0/D$, where ϕ_0 is the angular distance of the star from the direction normal to the baseline L . We note that:

- As the source position ϕ_0 changes, the fringe phase moves at an amplified rate Lu_0/D . The positional accuracy is therefore *magnified* by L/D .
- The fringe period remains set by the separation D of the secondary apertures no matter what is the separation L of the primary apertures on the outriggers.

SIM can be regarded as a Michelson stellar interferometer with two specific features:

- The separation D of the secondary apertures is reduced to zero⁴. The fringe period therefore becomes infinitely large, and the entire image of the star is either light or dark depending on the fringe phase.
- A delay $\Delta = L \sin\phi_0 + \delta$ is added to one side of the interferometer light path (e.g. between M_1 and M_2 in order to shift the double-slit pattern from u_1 back to within a small offset δ from the position of the star u_0 . This is necessary because of the finite bandwidth of the signal, which results in a limited coherence length, as discussed in Section 2.2.2. We will discuss the bandwidth effects on the fringe contrast later in this section.

The Fraunhofer pattern for a monochromatic point source in our one-dimensional model of SIM is therefore the square modulus of:

$$M(u) = 2 F(u - u_0) \cos(\pi(L \sin\phi_0 - \Delta)/\lambda), \quad (\text{A2})$$

which is

$$P(u) = |M(u)|^2 = P_0(u) (1 + \cos(2\pi\delta/\lambda)) \quad (\text{A3})$$

⁴Practical methods of achieving this beam combination usually introduce an additional fringe phase of typically $\approx \pi/4$ which we ignore here.

where $P_0(u) \equiv 2 |F(u - u_0)|^2$. Viewed as a function of the delay offset δ , this is a co-sinusoidal pattern with an average value set by the intensity P_0 of the star⁵, and varying from zero to $2P_0$. The fringe amplitude here is 1, appropriate for a point source.

Consider now an extended source in the sky, which we integrate in a direction perpendicular to the interferometer baseline in order to produce a 1-D image $B(\phi)$ where ϕ is an angle measured in the plane of the baseline (Fig. 17). Let us further assume that the position ϕ_0 to which we have initially offset the fringe pattern from our calibration grid star (by adding a delay Δ) is somewhere in the middle of $B(\phi)$. Each part $d\phi$ of the spatially-extended source then contributes a fringe pattern:

$$dP(\phi) = B(\phi)d\phi(1 + \Re e^{-2\pi i(L \sin \phi - \Delta)/\lambda}); \quad (\text{A4})$$

where again $\Delta = L \sin \phi_0 + \delta$ and \Re denotes the real part of the exponential. Let us further simplify the notation by assuming that the FOV is confined to a small region on the sky, so that $\sin \phi \approx \phi$, and measure L in wavelengths, $l = L/\lambda$. The total fringe pattern obtained by integrating equation A4 is then:

$$P = B_0 \Delta \phi + \Re \int_{-\infty}^{+\infty} B(\phi) e^{-2\pi i(l\phi - l\phi_0 - \delta/\lambda)} d\phi. \quad (\text{A5})$$

We can write the integral in this equation as:

$$B_0 \Delta \phi \times \Re e^{2\pi i(l\phi_0 + \delta/\lambda)} \times \Gamma(l), \quad (\text{A6})$$

where we recognize $\Gamma(l)$ as the Fourier transform of the normalized $B(\phi)$:

$$\Gamma(l) = \frac{\int_{-\infty}^{+\infty} B(\phi) e^{-2\pi i l \phi} d\phi}{B_0 \Delta \phi}. \quad (\text{A7})$$

Since $B(\phi)$ will in general not be symmetric about ϕ_0 , $\Gamma(l)$ will be complex, so we can write $\Gamma(l) = A(l) e^{2\pi i \phi(l)}$, leading to:

$$P = P_0 \{1 + A(l) \cos(2\pi(l\phi_0 - \phi(l) + \delta/\lambda))\}. \quad (\text{A8})$$

There are 3 unknowns here: the average power P_0 , the fringe amplitude $A(l)$, and the fringe phase $\phi(l)$ (measured here in turns). They can all be determined by measuring P as a function of delay δ . In practice, this can be achieved by continuously scanning δ over $\pm\lambda$, and recording P over a number of time intervals. This is the basis for our simulation of the measurement process and the introduction of photon noise, as will be described in appendix B.

Let us now consider the effects of the finite bandwidth of the interfering light. In order to keep the algebra manageable, we consider only the case of a plane wave from a point source. The fringe pattern we have derived in equation A3 will be different for different values of the wavelength λ . The total response is the sum of the fringe patterns for all wavelengths over the spectral range of the passband. Suppose the passband has a spectral shape $S(\nu)$. Then, in analogy to equation A4, that part of the spectrum at frequency ν contributes a fringe:

$$dP(\nu) = S(\nu) d\nu (1 + \Re e^{2\pi i(L \sin \phi_0 - \Delta)/\lambda}). \quad (\text{A9})$$

⁵The residual factor of 2 present in equation A2 is ignored further here. It comes in because we have doubled the collecting area by using two outrigger mirrors, and it will be subsumed into P_0 by the overall interferometer calibration procedure.

where $P_0 = S(\nu)d\nu$. We define a delay time $\tau = \delta/c$ where c is the speed of light. Then we have:

$$dP(\nu) = S(\nu)d\nu\{1 + \Re e^{-2\pi i\nu\tau}\}. \quad (\text{A10})$$

The total fringe pattern is obtained by integrating:

$$P = S_0\Delta\nu + \Re \int_{-\infty}^{+\infty} S(\nu)e^{-2\pi i\nu\tau}d\nu. \quad (\text{A11})$$

We recognize the integral as the Fourier transform $s(\tau)$ of the filter function $S(\nu)$. As an example, let's take a rectangular filter of height S_0 and width $\Delta\nu$ centered at ν_0 . The transform of this function is related by the shift theorem to the transform of a function $C(\nu)$ having the same shape but centered at the origin. The transform of $C(\nu)$ is $c(\tau) = S_0 \Delta\nu \text{sinc}(\pi\tau\Delta\nu)$, so the transform of $S(\nu) = C(\nu - \nu_0)$ is $s(\tau) = e^{2\pi i\nu_0\tau}c(\tau)$, and the fringe pattern becomes:

$$P(\nu) = S_0\Delta\nu\{1 + \text{sinc}(\pi\tau\Delta\nu) \cos(2\pi\nu_0\tau)\}, \quad (\text{A12})$$

so that if we scan $\delta = c\tau$ and record the intensity of the stellar image in the focal plane of SIM we will obtain the pattern shown in Figure 18.

B. Simulation of the measurement and its noise

In order to provide an estimate of SIM sensitivity and image quality, various noise components associated with the measurements need to be modeled as realistically as possible. The systematic (calibration) errors of the spacecraft are hard to predict at this time, because the design has not been finalized and a detailed hardware model is not yet available. As of now, we can only make assumptions on parameters such as fringe phase stability. On the other hand, the statistical errors due to photon statistics are straightforward to model. They are implemented in SIMSIM as follows.

The fundamental shape of the signal as a function of path difference (delay) between the two interfering beams has been derived in equation A8. Here, the term “signal” means the total number of photons falling on the detector over the integration time. If the delay δ is continuously modulated over $\pm\lambda$, then one can integrate the detector signal over four time “bins”, during each of which the delay moves over a quarter wave. This method has first been described by Wyant 1975 and was suggested for use in astronomical interferometers by Shao & Staelin (1977). It is usually referred to as the “quadrature method” and has been used in many ground-based interferometers. The usual implementation uses a triangular modulation of the delay with piezo-electric elements (e.g. Shao *et al.* 1988).

In ground-based interferometers the delay is scanned over the range of one wavelength in about 10 ms owing to the short coherence time of the atmospheric seeing, which otherwise moves the fringe phase ϕ in a random way. In principle, there is no need for high modulation frequencies in space, so that instead of a continuous modulation, one could envisage a “stop-and-stare” mode for the delay δ . However, since the continuous modulation technique is well established and simple to handle mathematically, we have used it to simulate the measurements in SIMSIM. Following Wyant 1975, the signal in the four bins $B1 \dots B4$ which, for mathematical simplicity have the limits $[-\lambda/8, \lambda/8]$, $[\lambda/8, 3\lambda/8]$, $[3\lambda/8, 5\lambda/8]$, and $[5\lambda/8, 7\lambda/8]$ can be calculated by integrating equation A8 over these intervals, yielding:

$$B1_{u,v} = P_0/4 + 1/(\pi\sqrt{2}) A(u,v) \sin\phi(u,v);$$

$$\begin{aligned}
 B2_{u,v} &= P_0/4 + 1/(\pi\sqrt{2}) A(u,v) \cos \phi(u,v); \\
 B3_{u,v} &= P_0/4 - 1/(\pi\sqrt{2}) A(u,v) \sin \phi(u,v); \text{ and} \\
 B4_{u,v} &= P_0/4 - 1/(\pi\sqrt{2}) A(u,v) \cos \phi(u,v).
 \end{aligned}$$

P_0 here is the total signal (in photons) in the FOV over the spectral passband during the integration time. In the case of a simulation, the values for the fringe amplitude and phase, $A(u,v)$ and $\phi(u,v)$, are known from the Fourier transform of the model source structure. Therefore, the values $B1 - B4$ can be calculated, and poisson noise can be added to them, before using the “measurements” to recover the source.

The noisy bin signals are then used to determine the “measured” fringe amplitude and phase according to

$$\begin{aligned}
 A_{\text{noisy}} &= \pi/\sqrt{2} \times \sqrt{(B1 - B3)^2 + (B2 - B4)^2} \\
 \phi_{\text{noisy}} &= \text{atan}\left(\frac{B1 - B3}{B2 - B4}\right)
 \end{aligned}$$

These values are re-entered in an empty array (the (u,v) -plane), and the (sparsely-filled) array is Fourier back-transformed to yield the reconstructed image of the source. As an option for the user, an additional noise component can be added that tries to model the expected phase calibration errors. Our simulations have shown, however, that up to the specified maximum error of 0.5° , this has negligible effects on the restoration quality. Since the PSF can also be computed, the recovered image can further be improved by applying restoration algorithms like CLEAN or MEM.

REFERENCES

Allen, R. J., Peterson, D., & Shao, M., 1997, SPIE Proc. 2871, 504

Crane, P. *et al.* 1993, AJ, 106, 1371

Fizeau, A. H. 1868, C. R. Acad. Sci. (Paris), 66, 943

Ford, H. C. *et al.* 1994, ApJ, 435, L27

Harms, R.J. *et al.* 1994, ApJ, 435, L35

Lagage, P.O. & Pantin, E. 1994, Nature, 369, 628

Lauer, T. R., *et al.* 1992, AJ, 103, 703

Macchetto, F., Marconi, A., Axon, D. J., Capetti, A., Sparks, W. B., & Crane, P. 1997, ApJ, 489, 579

Marconi, A., Axon, D. J., Macchetto, F. D., Capetti, A., Sparks, W. B., & Crane, P., 1997, MNRAS, 289, L21

Michelson, A. A. 1890, Phil. Mag., 30, 1

Michelson, A. A. & Pease, F.G. 1921, ApJ, 53, 249

Kalas, P. & Jewitt, D. 1996, AJ, 111, 1347

Kormendy, J. & Richstone, D. 1995, ARA&A, 33, 581

Reach, W. T., Franz, B. A., Kelsall, T., & Weiland, J. L. 1996, in AIP Conf. Proc. 348, “Unveiling the Cosmic Infrared Background”, ed. E. Dwek (New York: AIP), 37

Shao, M. & Staelin, D.H. 1977, J. Opt. Soc. Am., 67, 81

Shao, M. *et al.* 1988, A&A, 193, 357

Smith, B.A., Fountain, J.W., & Terrile, R.J. 1992, A&A, 261, 499

Traub, W. A. 1998, in “Proc. of Conference on Exo-Zodiacal Dust”, Ed. Backman, D.E. *et al.* NASA/CP-1998-10155, 129

Wyant, J. C. 1975, Appl. Opt., Vol. 14, No. 11, 2622

Fig. 1.— Left: example of a specific (u,v) -coverage, obtained from 170 SIM measurements. Right: the resulting point-spread-function.

Fig. 2.— Schematic view of SIMSIM capabilities .

Fig. 3.— Graphical User Interface of SIMSIM.

Fig. 4.— Model rotation curve for M 87.

Fig. 5.— Model surface brightness distribution after convolution with the “clean beam” for the $\text{H}\alpha$ line emission from a rotating gas disk around the black hole in M 87. The channels are 4 nm wide and centered at $[-8, -4, 0, 4, 8]$ nm offset from the line center.

Fig. 6.— Results of the simulated SIM synthesis imaging observations of the nucleus of M 87. The integration time was 100 s per baseline, and we used 170 baselines for a total on-source integration time of 5 hours. Shown are contour plots of the model source after convolution with the “clean beam” (top row), the direct Fourier inversion (center row), and the deconvolved Fourier inversion (bottom row) after 200 MEM iterations. A $0.05''$ region around the central bright continuum source has been masked **after** the simulation to better display the extended structure. Contour levels in all plots are 10, 20, 30...100% of the peak surface brightness, which is given below each plot in units of $10^{-13} \text{ ergs/s/cm}^2/\text{\AA}/\square''$

Fig. 7.— Profile plots for the model source (top), the direct Fourier inversion (middle), and the restored image after 200 MEM iterations (bottom).

Fig. 8.— Structure of the blueshifted wing of the $\text{H}\alpha$ emission (top), direct Fourier inversion (center), and reconstructed image after 200 MEM iterations (bottom) for black hole masses of $2, 3, 4 \cdot 10^9 M_\odot$. Contour levels are as in Fig. 6 .

Fig. 9.— Limiting black hole mass for the detection of a rotating gas disk around a black hole with SIM. The Doppler shift of the line has to be at least equal to the SIM channel width. This limit is shown as a function of black hole mass, disk inclination, and SIM spectral resolution. The solid lines refer to 4 nm wide SIM channels, dotted lines are for 1 nm channels, and dashed lines for 16 nm channel width. Four lines per set are shown, referring to disk inclinations of $i=0^\circ$ (edge-on), 20° , 40° , and 60° , the last being the highest curve of each set.

Fig. 10.— Surface brightness distribution of our zodiacal disk model. in face-on (left, $i = 90^\circ$) and edge-on orientation (right, $i = 0^\circ$). The grey scale is linear and identical in both plots to emphasize the higher surface brightness in the edge-on case. The central star has been removed for better contrast in the display.

Fig. 11.— Results of the SIMSIM reconstruction for a β Pic-like zodiacal disk oriented at an inclination of 0° (edge-on, left panel) and 90° (face-on, right panel). The columns in each panel are for distances of 100 pc (left column), 500 pc (center), and 1 kpc (right). The rows in each panel are for the input model after convolution with the “clean beam” (top row), the direct Fourier inversion (center row) and reconstructed image after 200 MEM iterations (bottom row). A $0.05''$ diameter region around the central star has been masked out **after** the simulation to better show the extended, low-level structure. All panels comprise a $0.3''$ field of view. Contour levels are 10, 20, 30...100% of the maximum (unmasked) surface brightness in each image (given below each panel in units of $10^{-15} \text{ ergs/s/cm}^2/\text{\AA}/\square''$). The assumed SIM nulling efficiency is $\epsilon = 10^{-4}$. Data were collected in five spectral channels (100 nm width between $\lambda = 500 \text{ nm}$ and $\lambda = 1000 \text{ nm}$)

and used for spectral synthesis imaging.

Fig. 12.— Results of the SIMSIM reconstruction for models with various dust content in the case of an edge-on (left) and face-on disk (right). The columns in each panel denote (from left to right): $C=1000, 100, 10$ times the solar dust content. Field size and contour levels are as in Fig. 11.

Fig. 13.— SIMSIM reconstructions of a β Pic- like system ($C=1000$) at a distance of 1 kpc. Shown are the results for various values of the SIM nulling efficiency ϵ . Again, the edge-on case is shown in the left panel and the face-on case on the right. The columns in each panel denote (from left to right): $\epsilon = 10^{-4}, 10^{-3}, 10^{-2}$. Field size and contour levels are as in Fig. 11.

Fig. 14.— SIMSIM reconstruction of a β Pic-like zodiacal disk ($C=1000$) at $d = 500$ pc without (top) and with (bottom) a 20 AU radius inner clear region. The central star has been masked **after** the simulation to better show the faint disk emission.

Fig. 15.— Sketch of Michelson’s stellar interferometer on the 100-inch telescope.

Fig. 16.— Focal plane profile of a star in Michelson’s stellar interferometer.

Fig. 17.— Geometry for collapsing a 2-D source onto the fringe normal direction.

Fig. 18.— SIM fringe pattern for a rectangular filter function.

Table 1. Input parameters for the M 87 model

Property		Ref.
stellar background	$\mu_I = 15.0 \text{ mag}/\square''$	1
central point source	$I = 16.1$	1
$\text{H}_\alpha + [\text{NII}]$ disk flux	$1 \cdot 10^{-12} \text{ ergs/cm}^2/\text{s}/\square''$	2
Radial intensity profile	$I(r) = A \cdot e^{r/0.1''}$	
black hole mass	$3 \cdot 10^9 M_\odot$	3
distance	16 Mpc	
inclination	45°	
position angle	0°	
grid resolution	$0.005''$	

Note. — References: 1) Lauer *et al.* 1992; 2) Harms *et al.* 1994, assuming a line ratio of $[\text{SII}]/(\text{H}\alpha + [\text{NII}]) = 4$; 3) Marconi *et al.* 1997.

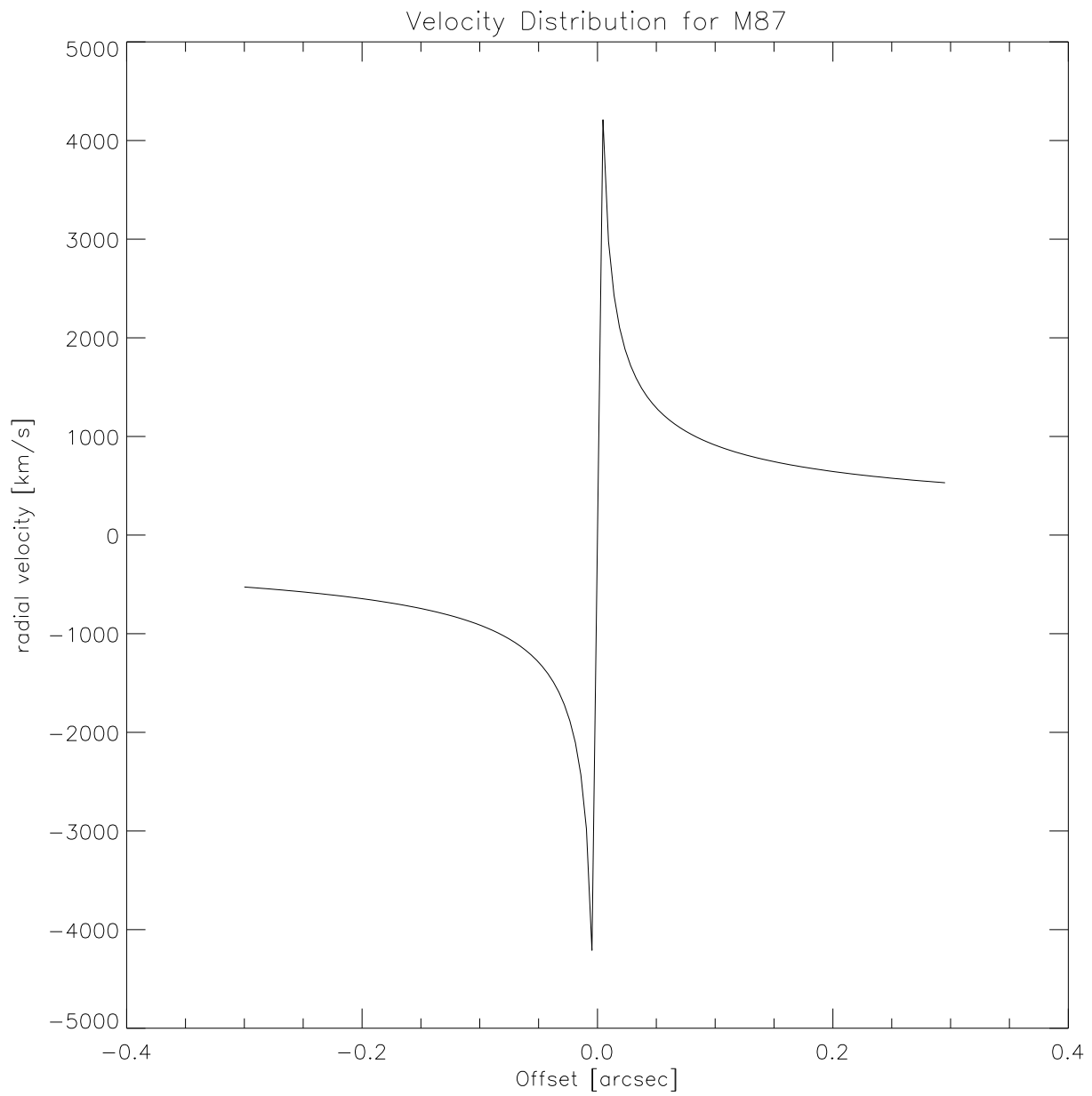


Fig. 4

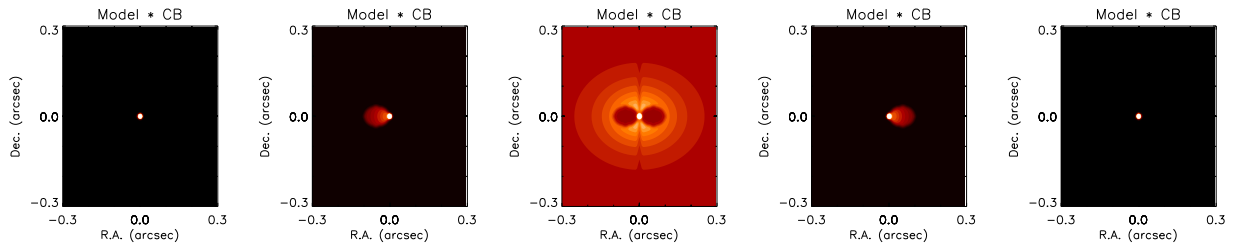


Fig. 5

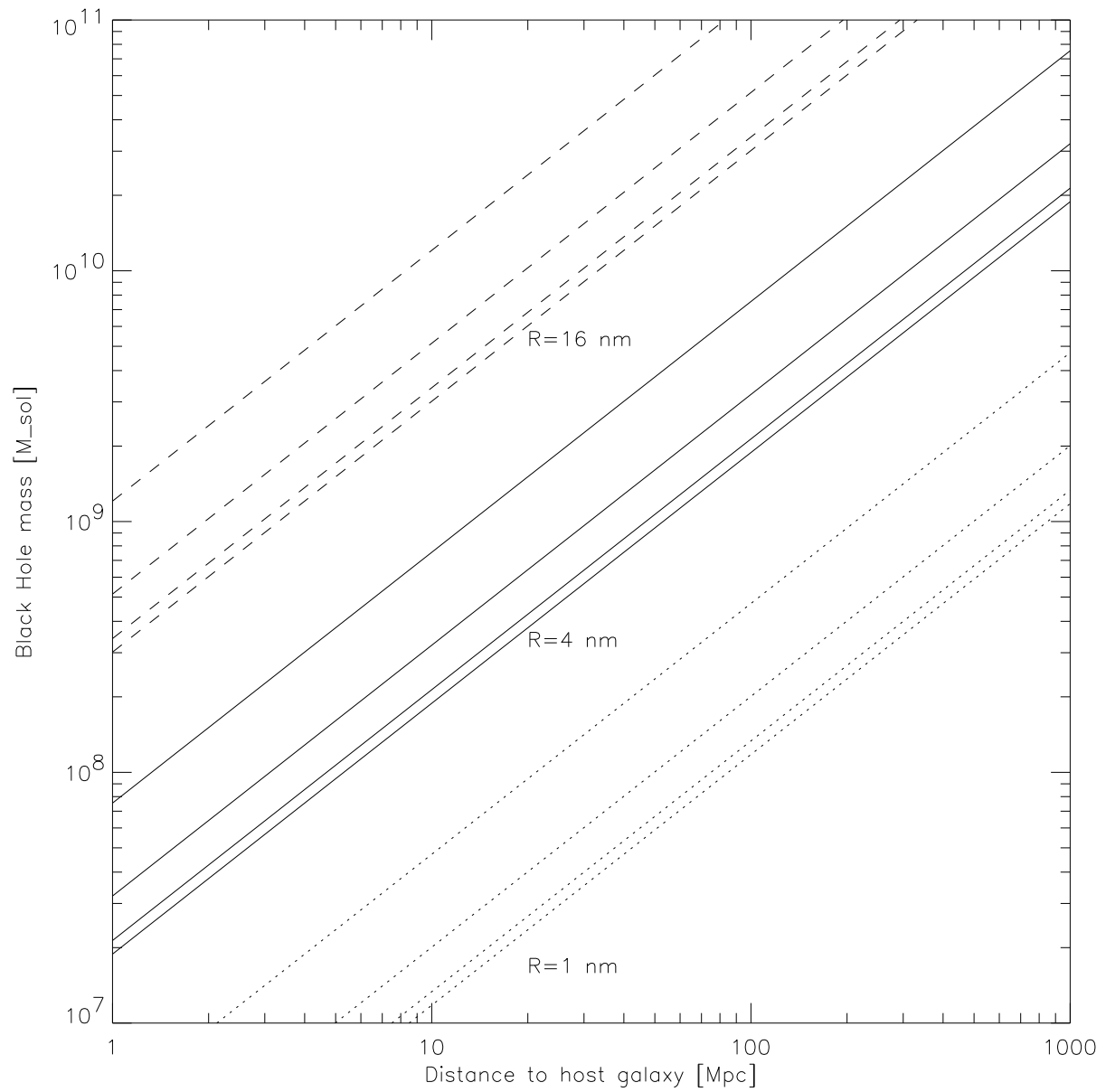
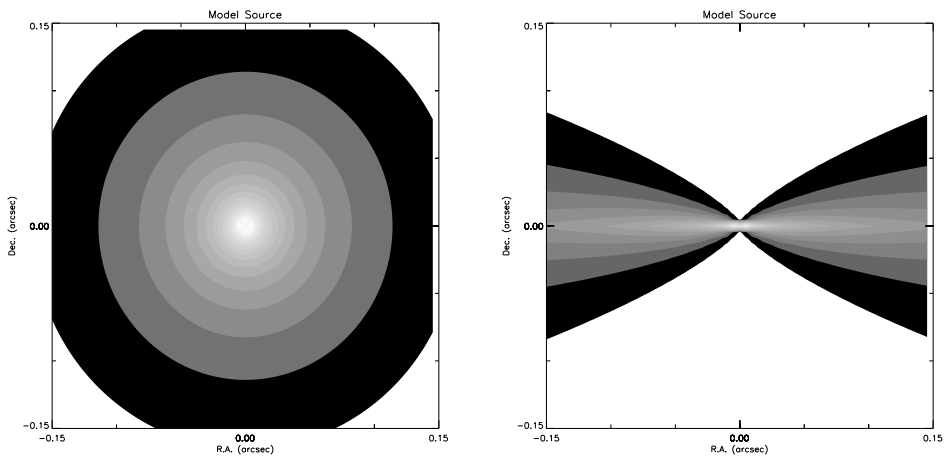


Fig. 9



Optical path of interferometer pencils

$M_1 - M_4$, mirrors
a, 100-inch paraboloid
b, convex mirror
c, coude' flat
d, focus

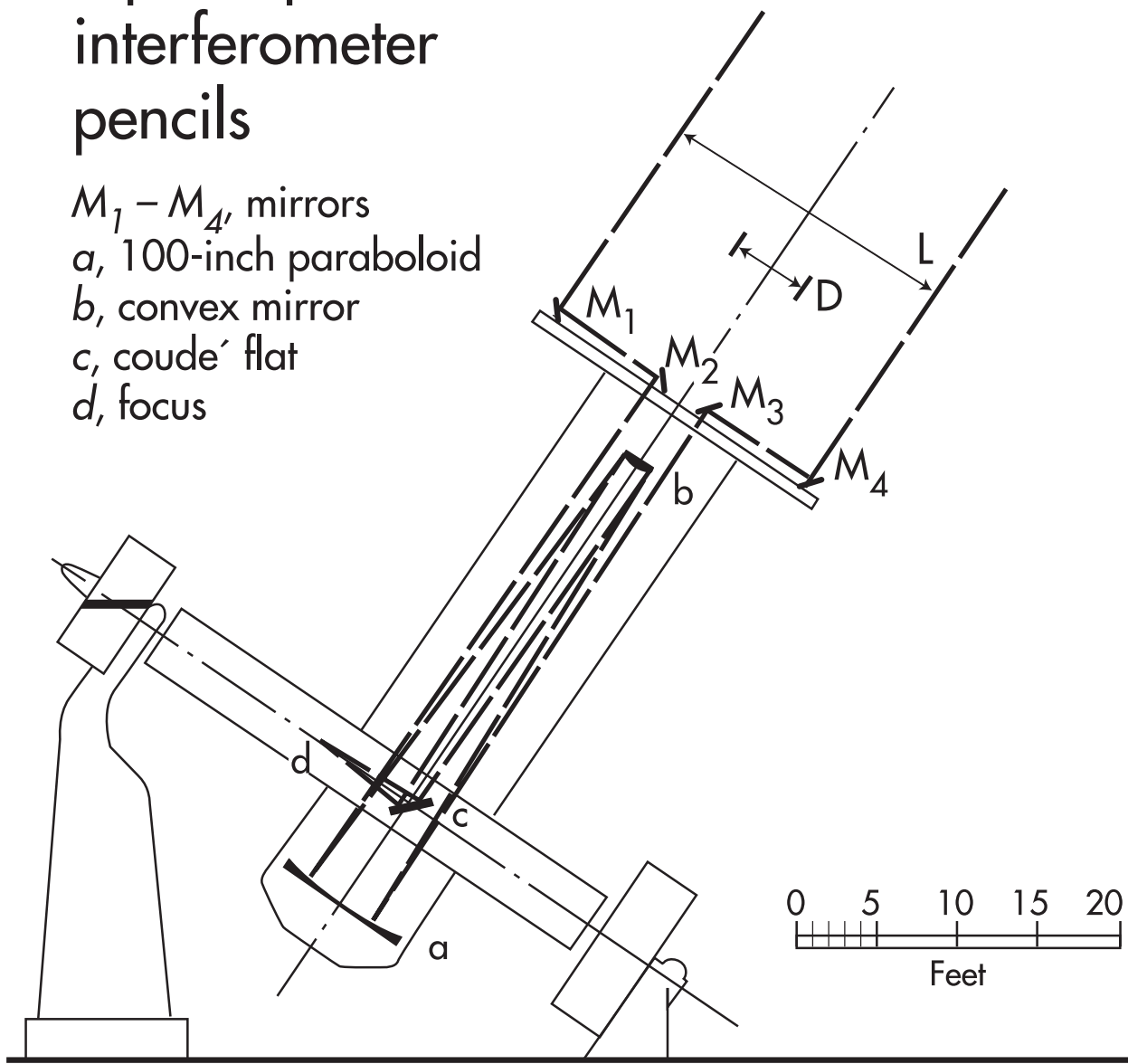


Fig. 15

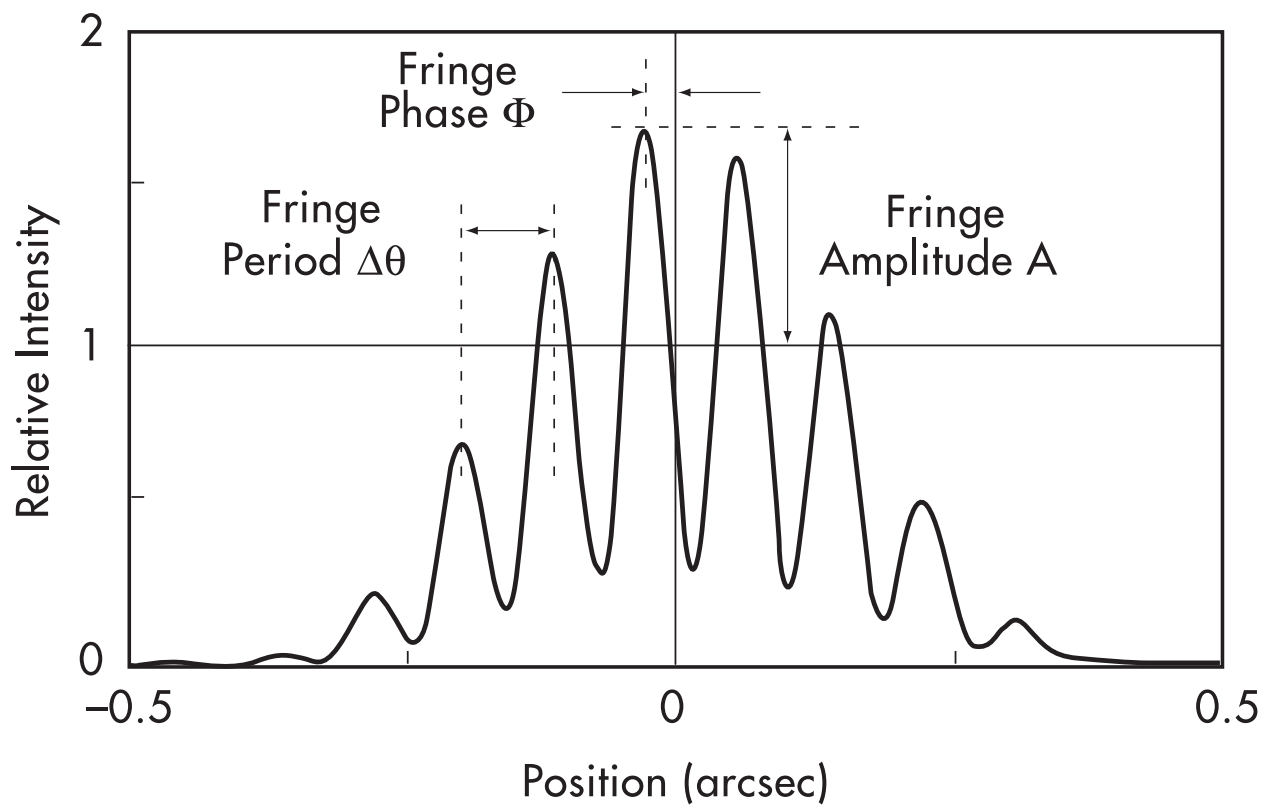


Fig. 16

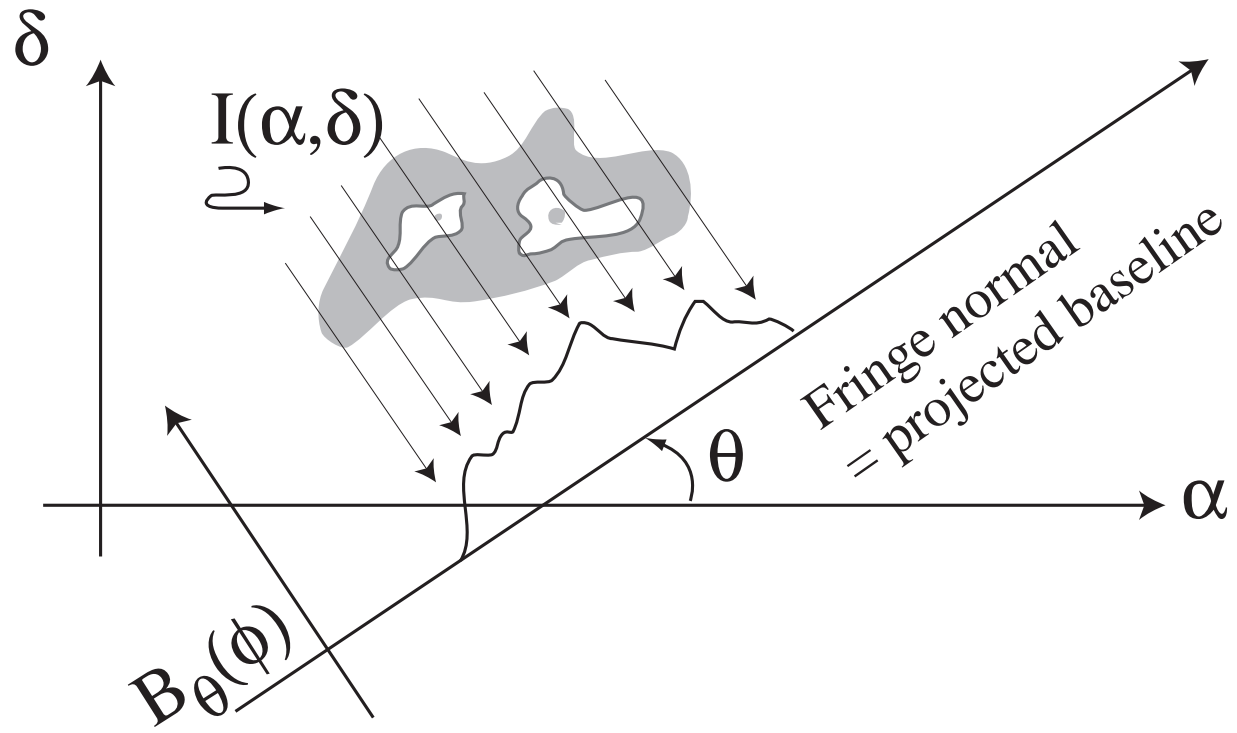


Fig. 17

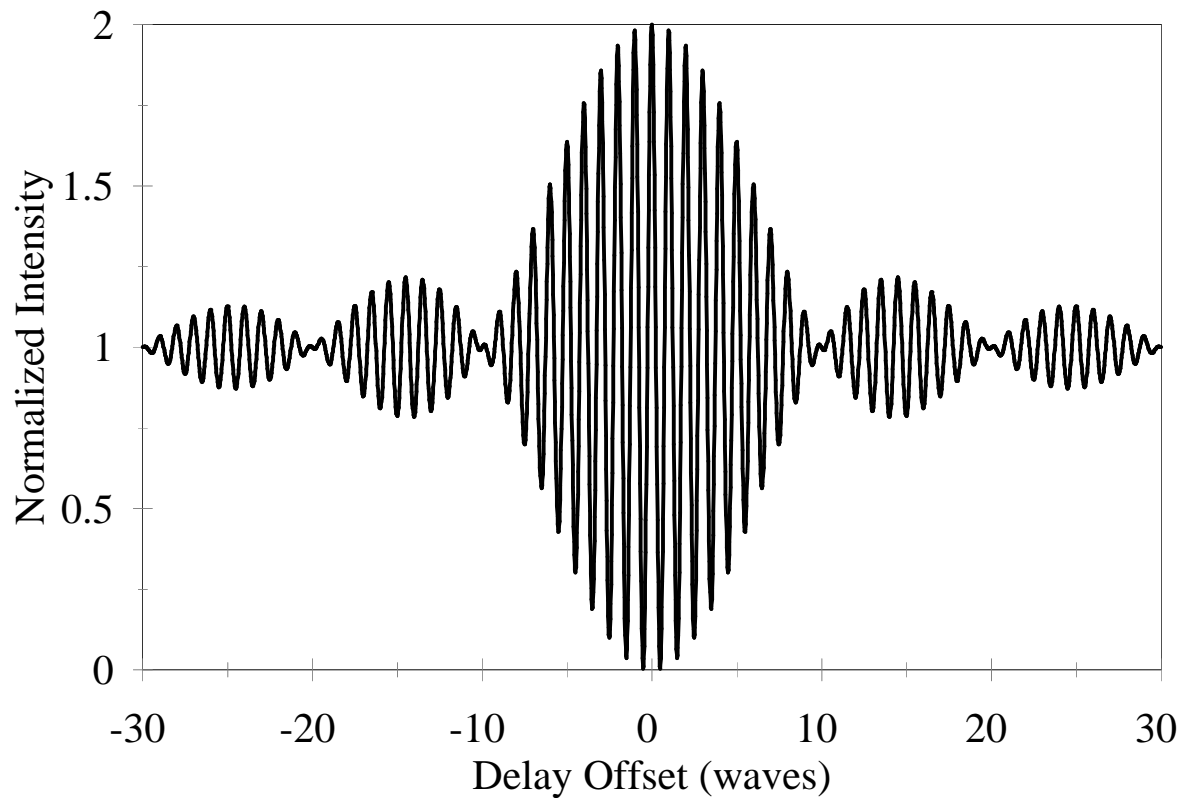


Fig. 18

This figure "fig1.gif" is available in "gif" format from:

<http://arxiv.org/ps/astro-ph/9903490v1>

This figure "fig2.gif" is available in "gif" format from:

<http://arxiv.org/ps/astro-ph/9903490v1>

This figure "fig3.gif" is available in "gif" format from:

<http://arxiv.org/ps/astro-ph/9903490v1>

This figure "fig6.gif" is available in "gif" format from:

<http://arxiv.org/ps/astro-ph/9903490v1>

This figure "fig7.gif" is available in "gif" format from:

<http://arxiv.org/ps/astro-ph/9903490v1>

This figure "fig8.gif" is available in "gif" format from:

<http://arxiv.org/ps/astro-ph/9903490v1>

This figure "fig11.gif" is available in "gif" format from:

<http://arxiv.org/ps/astro-ph/9903490v1>

This figure "fig12.gif" is available in "gif" format from:

<http://arxiv.org/ps/astro-ph/9903490v1>

This figure "fig13.gif" is available in "gif" format from:

<http://arxiv.org/ps/astro-ph/9903490v1>

This figure "fig14.gif" is available in "gif" format from:

<http://arxiv.org/ps/astro-ph/9903490v1>